Nano Research

Open Access

Research Article

Invisible to visible: Novel hydrophilic rare earth fluorescent composite inks for security applications

Tao Shen[1,2,3], Huanyu Zheng[1], Ruotong Liao[1], Bin Li[1,2,3], Juefei Wu[1], Zhengye Jiang[1], Xiaoyu Meng[1], and Cong Cao[1,2,3] ✉

[1] *School of Materials Science & Engineering, Zhejiang Sci-Tech University, Hangzhou 310018, China*
[2] *State Key Laboratory of Bio-based Fiber Materials, Zhejiang Sci-Tech University, Hangzhou 310018, China*
[3] *Zhejiang Sci-Tech University Shengzhou Innovation Research Institute, Shaoxing 312400, China*

Cite this article: *Nano Research*, **2025**, *18*, 94907380. https://doi.org/10.26599/NR.2025.94907380

ABSTRACT: Rare earth nanomaterials exhibit remarkable characteristics, including real-time responsiveness, luminescence stability, and multicolor emission capabilities. Herein, $NaYbF_4$:*x*%Tb,*y*%Eu@$NaYF_4$ core–shell structured nanoparticles (CSNP) were synthesized with distinct fluorescence under both ultraviolet (UV) and near-infrared (NIR) excitation. It can be uniformly mixed with a transparent ink solution and loaded into ink cartridges to print customized graphics on copy papers. The graphics cannot be recognized under normal visible light, and the concealed information with high resolution can only be exposed under specific excitation light. Combining with cryptography, it facilitates the implementation of advanced information encryption techniques. Consequently, the innovative fluorescent ink materials hold significant promise for enhancing anti-counterfeiting and information encryption.

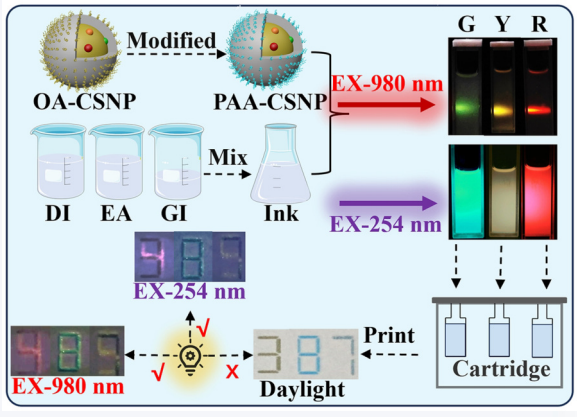

KEYWORDS: upconversion fluorescence, rare earth nanoparticles, fluorescent anti-counterfeiting ink, inkjet printing, multi-color

1 Introduction

The continuous emergence of fake and inferior products has significantly propelled the development of anti-counterfeiting technology, such as specialized paper [1], holography [2], watermarking [3], radio frequency identification (RFID), and fluorescence-based anti-counterfeiting [4, 5]. Despite the wide range of available technologies, each has its own limitations. For instance, although holographic labels are visually appealing, their susceptibility to physical replication significantly reduces their effectiveness in combating counterfeiting [6]. Specialized paper and watermarking have limited complexity and can be relatively easily replicated. Fluorescent anti-counterfeiting technology, in contrast, stands out for its strong security features, simple verification procedures, and high customizability. It provides a more secure and versatile solution at a reduced cost. This technology can be easily integrated with existing systems, such as quick response (QR) codes and American Standard Code for Information Interchange (ASCII) [7, 8], making it a widely adopted solution across various industries [9]. The unique excitation wavelength and sharp emission peak of fluorescent materials provide unparalleled advantages over conventional methods. Carbon quantum dots, semiconductor quantum dots, and organic dyes are common photoluminescent materials [10–12]. Although they have the potential for optical anti-counterfeiting, further regulation is still needed in terms of color purity of luminescence, multi-frequency switch ability, photobleaching and long-term stability. Among various fluorescent materials, rare earth ions have garnered significant attention for anti-counterfeiting due to their abundant and tunable emission spectra, high photostability, and stable physicochemical properties [13–15]. Mokhtar et al. generated patterns using the fluorescent signals of a mixture of rare earth ions and organic dyes [16], which are only visible under ultraviolet light. Cao et al. employed a screen printing technique to fabricate fluorescence-based anti-counterfeiting patterns by incorporating $NaYF_4$:Yb,Er nanoparticles into ink mixture [17]. The single excitation mode of these systems results in

Received: January 14, 2025; **Revised:** March 7, 2025
Accepted: March 17, 2025

✉Address correspondence to ccong@zstu.edu.cn

lower security for anti-counterfeiting, making it difficult to achieve higher-level anti-counterfeiting and information encryption [18–20].

To enhance the security of anti-counterfeiting, single-particle with multicolor integrating Stokes shift and anti-Stokes shift luminescence mechanisms have been explored. The $BaGdF_5$:Yb,Er,Tm nanoparticles exhibit tunable color under 980 nm excitation, but the ultraviolet emission signal at the corresponding 324 nm excitation remains constant and cannot be modulated [21]. Chen et al. achieved dual-mode luminescence by doping Eu^{3+} ions in the outer layer under the excitation at 273 and 976 nm [22]. Theoretical studies suggest that the core–shell architecture facilitates interfacial energy transfer through lattice matching effects, with the shell thickness playing a crucial role in determining the confinement strength of activator ions [23]. However, this core–shell structured material has a relatively narrow range of fluorescence color changes, which also limits its further application. In fact, the transition in fluorescence color has been achieved from green to yellow by varying the doping ratio of Tb^{3+} and Eu^{3+} ions in a core–shell configuration [24]. It inspired the creation multi-color emissions through the combination of such ions within single-particle. The doping ratio between the sensitizer and activator is a crucial factor in regulating multicolor luminescence [7]. An imbalance in the proportion of either component, whether too high or too low, can lead to cross-relaxation, which alters the fluorescence color and reduces the maximum energy transfer efficiency [25]. To enhance fluorescence efficiency, an inert shell layer has been recognized as an effective solution. This is achieved by isolating the quenching effects of the nucleus and surface ligands or solvent molecules, filling surface defects [26, 27]. Furthermore, rare earth nanomaterials require additional carriers to form anti-counterfeiting composite materials such as inks and hydrogels. Especially inks are considered the most effective method for constructing luminescent patterns for their high customizability, low cost, and suitability for mass production [28–30].

In this research, $NaYbF_4$:*x*%Tb,*y*%Eu@$NaYF_4$ core–shell structured nanoparticles were adopted and optimized to obtain precisely tunable fluorescence colors under dual excitation source. Firstly, the influence on fluorescence color of Tb^{3+} ions was investigated through adjusting doping concentration. Subsequently, different proportions of Eu^{3+} ions were introduced into nanoparticles to construct energy transfer from Tb^{3+} for red emission. An inert $NaYF_4$ shell was then deposited on the outer layer to enhance luminescence. Based on this, green fluorescence from Tb^{3+}, red fluorescence from Eu^{3+}, and their combined yellow fluorescence were obtained under dual excitation lights at 980 and 254 nm. Coated by polyacrylic acid (PAA) ligands and mixed with the special transparent ink, rare earth composite inks were obtained and loaded into printer cartridges without clogging, allowing for the printing of custom patterns with long-term stability and high resolution (Fig. 1). The output patterns can also be combined with ASCII cryptography to achieve more complex anti-counterfeiting and information encryption.

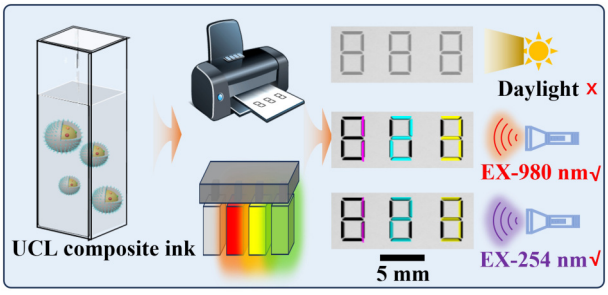

Figure 1 Synthesis of composite fluorescent ink materials with multicolor emission for use in inkjet printing anti-counterfeiting patterns under dual excitation resource, scale bar is 5 mm.

2 Results and discussion

2.1 Synthesis of rare earth doped nanoparticles

Tb^{3+} was firstly chosen as the energy donor along with Yb^{3+}. Prorok et al. demonstrated that Tb^{3+} exhibited strong two-photon upconversion emission at the $^5D_4 \rightarrow {}^7F_{(0-6)}$ transition through cooperation sensitizing upconversion (CSU) under 980 nm excitation [31]. Initially, a series of $NaYbF_4$:*x*%Tb (*x* = 5, 15, 30, 45) were synthesized using the solvent-thermal method as reported [32]. The particle size of the nanomaterials showed a decreasing tendency with increase in Tb ion concentration (Fig. S1 in the Electronic Supplementary Material (ESM)). When the concentration of Tb^{3+} ions reaches 30%, it achieves the strongest upconversion emission while maintaining a uniform morphology. Sotiriou et al. have provided a new approach [33], where Eu^{3+} can serve as a suitable energy acceptor from Tb^{3+}. Therefore, $NaYbF_4$:30%Tb,*y*%Eu nanoparticles (*y* = 0, 1, 5, 10, 15) were prepared with different concentrations of Eu^{3+} ions to obtain multicolor emissions. The diffraction peaks of X-ray diffraction (XRD) for the materials are basically consistent with the standard hexagonal phase $NaYbF_4$ (COD#00-027-1427) because of high doping Yb as matrix materials (Figs. S2(a)–S2(e) in the ESM). Furthermore, sharp diffraction peaks suggest good crystallinity of the nanoparticles. It is worth noting that the introduction of Eu^{3+} makes the particle size of the material gradually decrease (Fig. 2(a) and Table S1 in the ESM). This can be attributed to the important role of doping with different elements on morphology and crystal growth of nanocrystalline materials. High doping with heavy rare earth elements such as Yb^{3+} ions often results in large particle sizes, whereas materials dominated by light rare earth elements typically have reduced particle sizes [34, 35]. Prasad et al. attribute this phenomenon to the influence of surface charge density, which is triggered by the significant dipole polarizability [36]. Introducing light rare earth elements such as Eu^{3+} ions into $NaYbF_4$ nanocrystals, surface charge repulsion can be utilized to prevent the diffusion of F^- ions to the external surface during the crystal growth process [37].

By controlling the precursor feeding ratio (core:shell = 1:1) during the epitaxial growth process, a $NaYF_4$ shell with a thickness of 1.5–11.0 nm was deposited on the surface (Table S1 in the ESM). Based on the analysis of the XRD diffraction patterns and standard cards, the core–shell structured nanomaterial corresponds to the hexagonal phase $NaYF_4$ (COD#00-016-0334) crystal structure (Fig. S2(f) in the ESM). Compared with $NaYbF_4$:30%Tb,*y*%Eu, the larger ionic radius of Y^{3+} induces more pronounced lattice expansion, resulting in an increase in interplanar spacing, which manifests as a shift of diffraction peaks toward lower angles in X-ray diffraction patterns. The size of core–shell structured nanomaterials also increased obviously than core nanoparticles (Fig. 2(b) and Table S1 in the ESM). Additionally, high-resolution transmission electron microscopy (HRTEM) images showed clear lattice fringe of

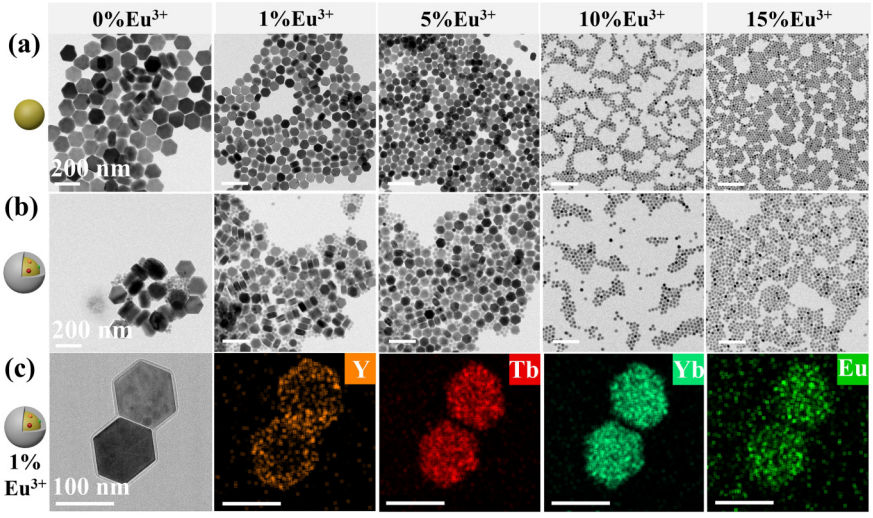

Figure 2 TEM images of (a) $NaYbF_4$:30%Tb,*y*%Eu nanoparticles and (b) CSNP:*y*%Eu nanoparticles (*y* = 0, 1, 5, 10, 15). (c) STEM image of CSNP:1%Eu nanoparticles and corresponding Y, Tb, Yb, and Eu element diagrams.

0.52 nm, associated with the (100) face in β-$NaYF_4$ (Figs. S3(a) and S3(b) in the ESM). Scanning transmission electron microscopy (STEM) images indicate that Y^{3+} ions were mainly distributed at the edge of the nanocrystal, while Yb^{3+}, Tb^{3+}, and Eu^{3+} ions were uniformly distributed in the central region (Fig. 2(c)). Furthermore, the energy dispersive X-ray spectrometer (EDS) line scan analysis of CSNP:1%Eu nanoparticles showed that the position of elements is also consistent with STEM results, showing the successful synthesis of core–shell structure (Fig. S3(c) in the ESM).

2.2 Multicolor luminescence of rare earth doped nanoparticles

Firstly, the UCL properties of $NaYbF_4$:*x*%Tb nanoparticles (*x* = 5, 15, 30, 45) were examined under 980 nm excitation (Fig. S4(a) in the ESM). The excitation energy was initially absorbed by Yb^{3+} ions and transferred to the nearby Tb^{3+} ions through CSU. Then the $^5D_4$ energy level of Tb^{3+} is filled, resulting in two strong green emission peaks at 488 and 541 nm, as well as two orange emissions at 582 and 618 nm, corresponding to the transitions of $^5D_4 \rightarrow {}^7F_3$, $^5D_4 \rightarrow {}^7F_4$, $^5D_4 \rightarrow {}^7F_5$, and $^5D_4 \rightarrow {}^7F_6$ (Figs. S4(b) and S4(c) in the ESM). As the Tb^{3+} doping concentration increased, the fluorescence intensity of the nanomaterials also increased, peaking at 30% Tb^{3+} ion doping. While at a molar ratio of 45% Tb^{3+}, concentration quenching effect occurs, leading to a significant decrease in fluorescence. The adjustment of Tb^{3+} and Yb^{3+} doping alone did not bring about a change in fluorescence color through Commission Internationale de l´Eclairage (CIE) chrominance cards (Fig. S4(d) in the ESM), so that the energy receiver Eu^{3+} was subsequently introduced to achieve red luminescence. Under 980 nm excitation, with the increase of Eu^{3+} ion, the upconversion emissions of Tb^{3+} ions at 488 and 540 nm show a significant attenuation, decreasing to 15% of the original intensity (Fig. S5(a) in the ESM). It demonstrated the effective energy transfer between donor Tb^{3+} and acceptor Eu^{3+} (Fig. 3(a)). Zhou et al. has proposed the energy transfer pathway from Tb^{3+} to Eu^{3+}[24], enhancing the fluorescence of Eu by inhibiting the fluorescence of Tb to achieve color regulation. The upconversion emission peaks at 590, 615, and 685 nm were corresponding to the transition of $^5D_0 \rightarrow {}^7F_0$, $^5D_0 \rightarrow {}^7F_2$, and $^5D_0 \rightarrow {}^7F_4$. As the doping concentration of Eu^{3+} increases, the upconversion emission of Eu first strengthens and then decays, reaching its peak at 5%.

The nanomaterials exhibited similar peaks with the upconversion emission and significant color differences under 254 nm excitation (Fig. S5(b) in the ESM). A more evident color change from green to red is obtained by analyzing the CIE color card corresponding to the materials (Figs. S6(a) and S6(b) in the ESM). When the concentration of Eu^{3+} reaches 10% and 15%, the color of the material tends to be stable and no longer shows significant changes. To protect the fluorescence, an inert shell of $NaYF_4$ was employed to shield the core material from non-radiative attenuation induced by surface defects and solvents. Notably, the $NaYF_4$ shell effectively confined the activator ions (Eu^{3+} and Tb^{3+}) within the core region, suppressing concentration quenching even at high doping levels (10%–15%). The core–shell structured nanoparticles have bright fluorescence and four characteristic peaks, which have similar trend with core nanoparticles (Figs. 3(b) and 3(e)). This spectral consistency confirms that the shell thickness does not alter electronic transition but solely passivates surface defects, as evidenced by unchanged CIE coordinates. From the fluorescence photos and CIE color cards, the material indeed transitions from green to red by adjusting Eu^{3+} doping, without changing the color after coating $NaYF_4$ layer (Figs. 3(c) and 3(d), and Figs. S6(c) and S6(d) and Tables S2 and S3 in the ESM).

2.3 Preparation of hydrophilic composite inks

PAA contains abundant carboxylic acid groups that bind to particle surfaces, enhancing material hydrophilicity. These groups form interpolymer complexes through hydrogen bonding, creating strong adhesion essential for homogeneous ink formulation [38]. Therefore, PAA is modified on the material surface through ligand exchange to replace hydrophobic oleic acid ligands. The XRD diffraction peaks and TEM image demonstrated that the modification of PAA did not change the crystal structure and the morphology (Figs. S2(g) and S7(a) in the ESM). The PAA-CSNP exhibit a significant optical signal attenuation at 660 nm while essentially maintaining the constant luminescence color. Even after 240 days, PAA-CSNP still maintained 95% of its original fluorescence intensity (Fig. 4(a) and Fig. S7(b) in the ESM). Such excellent photostability could guarantee the clarity and storage resistance of printed patterns.

It is worth noting that under 254 nm excitation, the fluorescence

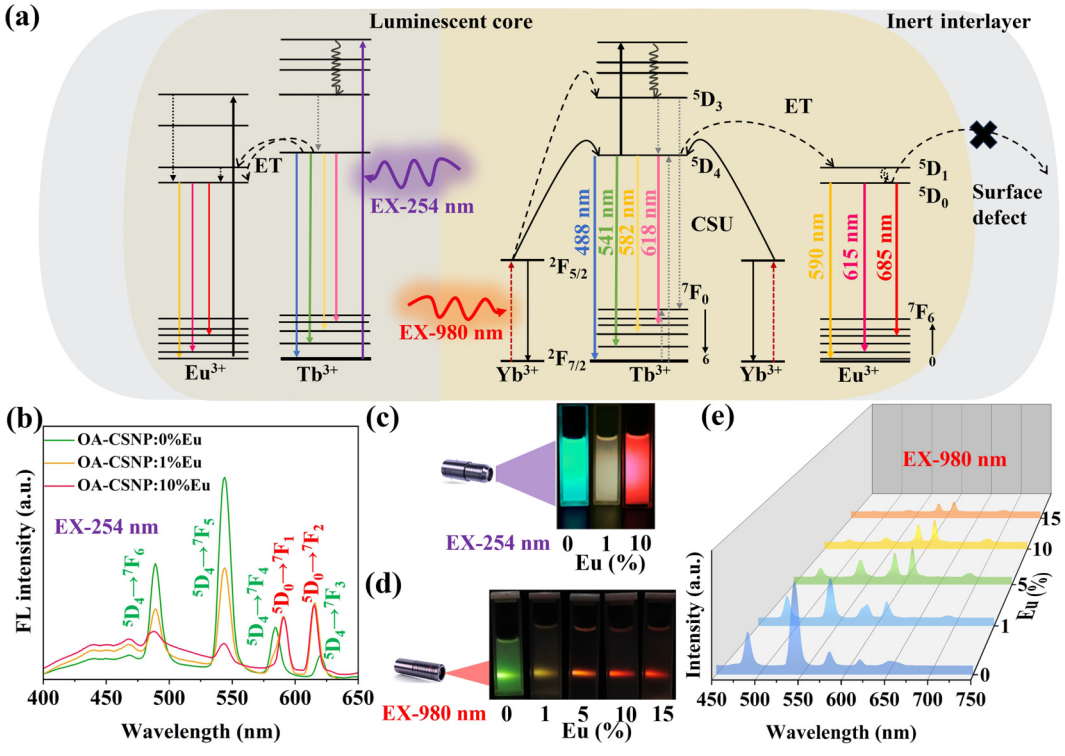

Figure 3 (a) Energy level diagrams of multicolor luminescent nanoparticles under dual excitation lights. (b) Fluorescence spectra and (c) photos of OA-CSNP:*y*%Eu (*y* = 0, 1, 10) under 254 nm excitation. (d) Photos and (e) upconversion fluorescence spectra of OA-CSNP:*y*%Eu (*y* = 0, 1, 5, 10, 15) under 980 nm excitation.

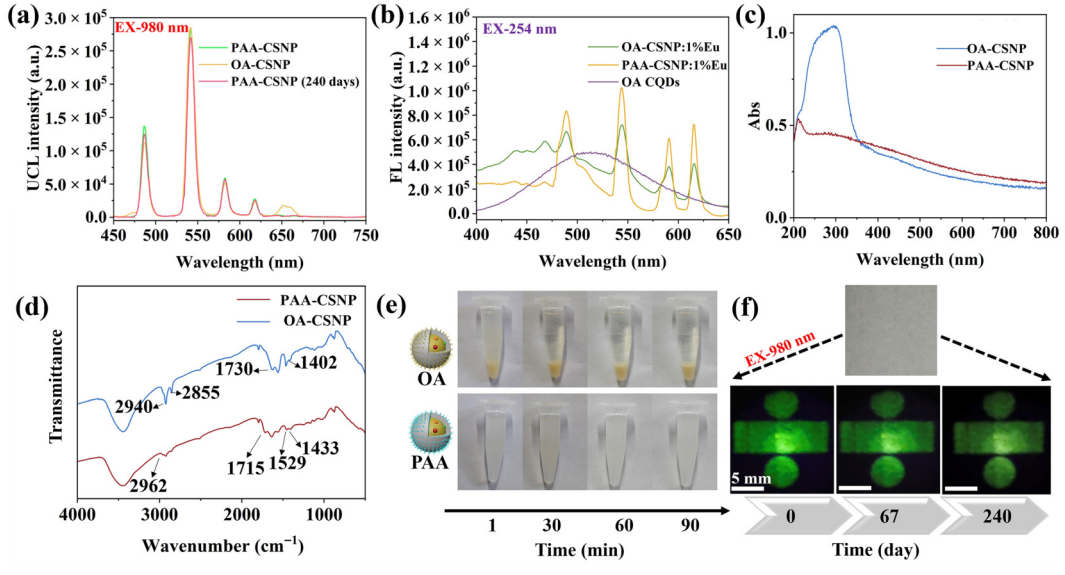

Figure 4 (a) The fluorescence spectra of OA-CSNP, PAA-CSNP, and PAA-CSNP for 240 days under 980 nm excitation. (b) Fluorescence spectra of OA-CSNP, PAA-CSNP, and OA CQDs excited under 254 nm. (c) Solid UV–vis absorption spectra of CSNP with two different ligands. (d) The FTIR data of OA-CSNP and PAA-CSNP. (e) Dispersibility of CSNP with different surface ligands in inks over times. (f) The photos of the same fluorescent pattern after a period of time.

of PAA-CSNP even enhanced than OA-CSNP. Additionally, the broad peak in the 450–600 nm region for OA-CSNP was absent in PAA-CSNP (Fig. 4(b)). The OA-CSNP materials have strong absorption peaks in the range of 200–350 nm (Fig. 4(c)). Wu et al. once used a high-temperature carbonization method to heat oleic acid to produce carbon quantum dots (OA CQDs). The OA CQDs have strong pale blue light emission under 254 nm excitation [39]. Accordingly, after heating to 300 °C for 1 h and cooled down, the pure oleic acid solution surely exhibited a peak shape similar with OA-CSNP under 254 nm excitation (Fig. 4(b)). While the untreated oleic acid solution did not emit any fluorescence in the same condition (Fig. S8 in the ESM). It indicated that the OA CQDs are formed during the synthesis of OA-CSNP, which affect the fluorescence signals in solutions under 254 nm excitation. Fourier transform infrared spectroscopy (FTIR) was utilized to analyze the functional groups of the CSNP (Fig. 4(d)). It was evident that the surface of CSNP was effectively coated with PAA.

In terms of viscosity and surface tension, deionized water,

anhydrous ethanol, and glycerol were combined in a 2:2:1 mass ratio to form transparent inks suitable for inkjet printing [40]. Furthermore, the OA-CSNP exhibited significant precipitation after directly mixing with inks for 1 min and longer (Fig. 4(e)). In contrast, the modified PAA-CSNP remained stable when mixed with inks, showing no notable precipitation at various time points. It demonstrated the excellent water solubility and compatibility of the modified nanoparticles with transparent inks. To minimize interference, PAA-CSNP:0%Eu (green), PAA-CSNP:1%Eu (yellow), and PAA-CSNP:10%Eu (red) were selected from specific proportion based on the fluorescence intensities and added to cartridges to form corresponding fluorescent inks (Table S4 in the ESM).

2.4 Information storage and anti-counterfeiting applications

Composite fluorescent inks were utilized to print designed patterns on A4 papers. According to the principle of printers, green fluorescence was designated as cyan, yellow fluorescence as yellow, and red fluorescence as magenta. For instance, one could change the pattern design with cyan on the computer to print green fluorescent pattern. It showed clear and bright green upconversion signals even after 240 days (Fig. 4(f)). A cyan QR code pattern was also designed and subsequently printed (Fig. 5(a)). The printed pattern was invisible and concealed under daylight. However, upon excitation with 980 or 254 nm light, the pattern became visible and could be recognized with a smartphone. Meanwhile the OA-CSNP and PAA-CSNP were evaluated by detecting emission peaks of 541 nm, showing excellent stability under dual excitation lights (Fig. 5(b)). As shown in Fig. 6(a), the paper displayed the incorrect information of "3 8 7" under daylight. When illuminated with a 980 or 254 nm light, the true information of "4 8 5" became visible.

Subsequently, the precision of printed patterns was evaluated. The standard resolution card is shown and printed under excitation at 980 nm in bright environment (Fig. S9 in the ESM). After one, three, and five reprints for this pattern, corresponding fluorescent photos were taken in a darkroom (Fig. 6(b)). With a single layer, the pattern was dim but clear. With five printing layers, the pattern was bright but decreased resolution. The pattern showed excellent resolution and improved light after three repeated layers, making it more suitable for producing anti-counterfeiting patterns. To enhance the confidentiality and information loading of patterns, a logical encryption strategy was implemented by combining three fluorescent inks with ASCII (Fig. 6(c)). Specifically, the encoding protocol assigns binary values based on fluorescent colors: green represents "1", while yellow and red represent "0". For example, the binary code "0" is encoded in the first cell of the first row as yellow, followed by green ("1") and red ("0") (from left to right). By arranging fluorescent dots in predefined sequences (spatial positions from left to right), the decoded encrypted information is 'ZSTU' (Table S5 in the ESM). The hidden information could only retrieve under both 254 and 980 nm excitation combined with a logical decoding algorithm that maps color sequences to ASCII values. QR code assisted by smartphones and logical information encryption strategy is practical for using such composite inks. It can expand the anti-counterfeiting application of rare earth nanocrystals.

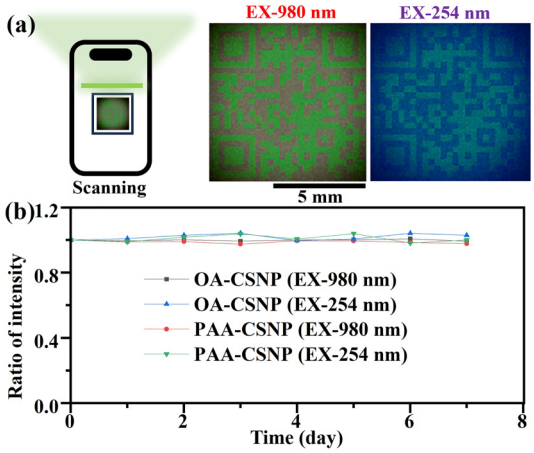

Figure 5 (a) Fluorescent photos of QR patterns were taken by a smartphone under two excitation modes. (b) OA-CSNP and PAA-CSNP at the emission peak of 541 nm under 254 and 980 nm excitation.

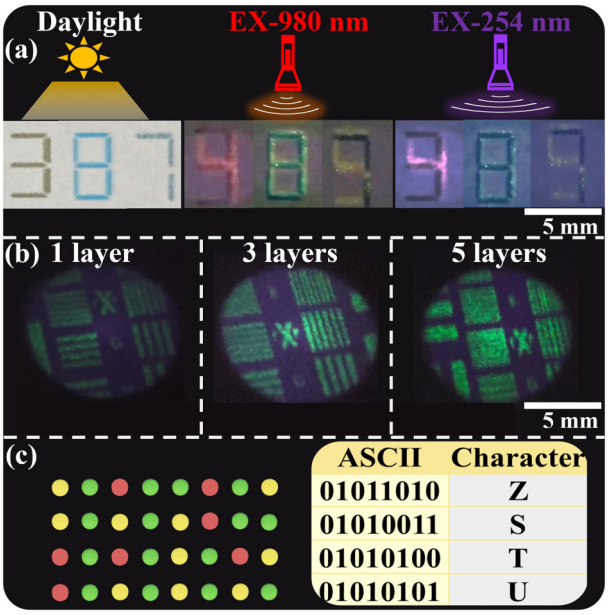

Figure 6 (a) The photos of pattern were taken by a smartphone under daylight, 980 nm excitation and 254 nm excitation. (b) Under 980 nm excitation, the fluorescence image was captured in a dark room after one, three, and five reprints. (c) A schematic diagram of information encryption based on multicolor fluorescent patterns and ASCII logical encoding.

3 Conclusions

This study successfully formulated anti-counterfeiting composite inks by utilizing rare earth doped fluorescent nanomaterials and integrating logical encryption strategies. The printed patterns demonstrated fluorescent emissions under distinct excitation wavelengths (980 and 254 nm), while remaining invisible under daylight. This unique feature significantly augments the concealment and security of information embedded within the QR codes. Moreover, by combining three fluorescent colors of composite inks with ASCII coding, a robust encryption methodology has been established for precise decoding of information retrieval. This research not only elucidates the use of multicolor rare earth nanoparticles in anti-counterfeiting applications, but also highlights their potential in secure information transmission scenarios.

4 Methods

4.1 Synthesis of rare earth doped nanoparticles

The $NaYbF_4$:*x*%Tb (*x* = 5, 15, 30, 45) and $NaYbF_4$:30%Tb,*y*%Eu (*y* = 0, 1, 5, 10, 15) core nanoparticles were synthesized as the same method as follows. Take $NaYbF_4$:30%Tb,10%Eu as an example: 1 mmol of rare earth chlorides (0.60 mmol $YbCl_3$, 0.30 mmol $TbCl_3$, and 0.10 mmol $EuCl_3$), 1-octadecene (15 mL), and oleic acid (6 mL) were mixed and stirred in a flask. The mixture was heated to 130 °C and vacuumed for 30 min. After completely dissolved and cooled to 40 °C, methanol solution containing NH_4F (4.0 mmol) and NaOH (2.5 mmol) was added, followed by heating to 110 °C and vacuuming for 40 min. The solution was heated to 300 °C under nitrogen for 1 h. After cooling, core nanoparticles were centrifugated and redispersed in cyclohexane.

$NaYbF_4$:30%Tb,*y*%Eu@$NaYF_4$ was prepared with the similar method. It involved mixing 0.5 mmol of the aforementioned core material and 0.5 mmol of $YbCl_3$ in oleic acid and 1-octadecene solvents. Except for the addition of such reaction materials, the other experimental steps were basically consistent with the synthesis of the core material.

4.2 Preparation of fluorescent composition inks

The hydrophilic PAA was modified on the material surface through ligand exchange. 10 mL of cyclohexane containing 0.5 mmol of OA-CSNP and 10 mL of ethanol containing 1.58 g of PAA were mixed at 30 °C for 24 h. Then, the PAA-CSNP was obtained by centrifuging, washing, and vacuum drying. To obtain fluorescent composite inks, a mixture of ethanol, deionized water, and glycerol (mass ratio of 2:2:1) was stirred and sonicated with PAA-CSNP solutions for 30 min. Then the original ink from the color cartridges was removed and washed with ethanol and deionized water. And the corresponding fluorescent inks were put into the cartridge holes for cyan, magenta, and yellow. Finally, the color pattern on the computer was designed and printed according decoding.

Electronic Supplementary Material: Supplementary material (figures of TEM images, XRD patterns, HRTEM image, fluorescence spectra, EDS line scan analysis, CIE cards, and tables for fluorescent inks) is available in the online version of this article at https://doi.org/10.26599/NR.2025.94907380.

Data availability

All data needed to support the conclusions in the paper are presented in the manuscript and the Electronic Supplementary Material. Additional data related to this paper may be requested from the corresponding author upon request.

Acknowledgements

This work was supported by the National Natural Science Foundation of China (Nos. 22101257 and 52103189) and Foundation of Zhejiang Sci-Tech University Shengzhou Innovation Research Institute (No. SYY2024B000001).

Declaration of competing interest

All the contributing authors report no conflict of interests in this work.

Author contribution statement

T. S.: Data curation, writing – original draft, software. H. Y. Z.: Validation, experimental design. R. T. L.: Data curation. B. L.: Conceptualization, writing manuscript. J. F. W.: Software, data curation. Z. Y. J.: Validation. X. Y. M.: Experimental design. C. C.: Funding acquisition, supervision, writing – review and editing. All the authors have approved the final manuscript.

Use of AI statement

None.

References

[1] Ren, G. H.; Zhu, Z. J.; Zhang, J. B.; Zhao, H. W.; Li, Y. F.; Han, J. G. Broadband terahertz spectroscopy of paper and banknotes. *Opt. Commun.* **2020**, *475*, 126267.

[2] Chen, G. N.; Wei, W.; Li, S.; Zhou, X. P.; Li, Z. A.; Peng, H. Y.; Xie, X. L. Liquid crystal-assisted manufacturing of flexible holographic polymer nanocomposites for high-security level anticounterfeiting. *Mater. Chem. Front.* **2022**, *6*, 3531–3542.

[3] Ju, L.; Gao, W. B.; Zhang, J. Y.; Qin, T. Y.; Du, Z.; Sheng, L.; Zhang, S. X. A. A new absorption/fluorescence dual-mode hydrochromic dye for water-jet printing and anti-counterfeiting applications. *J. Mater. Chem. C* **2020**, *8*, 2806–2811.

[4] Cheung, H. H.; Choi, S. H. Implementation issues in RFID-based anti-counterfeiting systems. *Comput. Ind.* **2011**, *62*, 708–718.

[5] Liu, S. Q.; Wang, J.; Tang, F.; Wang, N.; Li, L.; Yao, C.; Li, L. D. Aqueous systems with tunable fluorescence including white-light emission for anti-counterfeiting fluorescent inks and hydrogels. *ACS Appl. Mater. Interfaces* **2020**, *12*, 55269–55277.

[6] Abdollahi, A.; Roghani-Mamaqani, H.; Razavi, B.; Salami-Kalajahi, M. Photoluminescent and chromic nanomaterials for anticounterfeiting technologies: Recent advances and future challenges. *ACS Nano* **2020**, *14*, 14417–14492.

[7] Zhang, J.; Cao, C.; Wang, J. S.; Li, S. W.; Xie, Y. $NaYF_4$:Yb,Er@$NaYF_4$:Yb,Tm and $NaYF_4$:Yb,Tm@$NaYF_4$:Yb,Er core@shell upconversion nanoparticles embedded in acrylamide hydrogels for anti-counterfeiting and information encryption. *ACS Appl. Nano Mater.* **2022**, *5*, 16642–16654.

[8] Zhang, J. C.; Pan, C.; Zhu, Y. F.; Zhao, L. Z.; He, H. W.; Liu, X. F.; Qiu, J. R. Achieving thermo-mechano-opto-responsive bitemporal colorful luminescence via multiplexing of dual lanthanides in piezoelectric particles and its multidimensional anticounterfeiting. *Adv. Mater.* **2018**, *30*, 1804644.

[9] Zhang, C. Y.; Yin, Q. X.; Ge, S. K.; Qi, J. X.; Han, Q. Y.; Gao, W.; Wang, Y. K.; Zhang, M. D.; Dong, J. Optical anti-counterfeiting and information storage based on rare-earth-doped luminescent materials. *Mater. Res. Bull.* **2024**, *176*, 112801.

[10] Wen, Y. H.; Sheng, T. L.; Zhu, X. Q.; Zhuo, C.; Su, S. D.; Li, H. R.; Hu, S. M.; Zhu, Q. L.; Wu, X. T. Introduction of red-green-blue fluorescent dyes into a metal-organic framework for tunable white light emission. *Adv. Mater.* **2017**, *29*, 1700778.

[11] Yu, Y. T.; Ma, T. Y.; Huang, H. W. Semiconducting quantum dots for energy conversion and storage. *Adv. Funct. Mater.* **2023**, *33*, 2213770.

[12] Yuan, Y.; Bao, X. M.; Wu, L. L.; Zhou, M.; Yu, Y. Y.; Wang, Q.; Wang, P. Solvent-regulated synthesis of full-color fluorescent nitrogen/sulfur co-doped carbon quantum dots for anti-counterfeiting textiles. *Chem. Eng. J.* **2024**, *493*, 152488.

[13] Gao, Y. Y.; Yang, Y. H.; Wei, Y. H.; Li, Y. Q.; Cai, H. T.; Wu, C. H. Manipulating dynamic fluorescent emissions by introducing SP molecule into functionalized HOFs and application in time-resolved information encryption. *Adv. Funct. Mater.* **2025**, *35*, 2416025.

[14] Wei, Y. H.; Zhu, J. K.; Gao, Y. Y.; Cai, H. T.; Wu, C. H.; Yang, Y. H.; Zhu, G. C.; Khabibulla, P.; Kayumov, J. Novel core–shell materials SiO_2@Tb-MOF for the incorporation of spiropyran molecules and its application in dynamic advanced information encryption. *J. Colloid. Interface. Sci.* **2025**, *680*, 224–234.

[15] Suo, H.; Zhu, Q.; Zhang, X.; Chen, B.; Chen, J. K.; Wang, F. High-security anti-counterfeiting through upconversion luminescence. *Mater. Today Phys.* **2021**, *21*, 100520.

[16] Mokhtar, O. M.; Attia, Y. A.; Wassel, A. R.; Khattab, T. A. Production of photochromic nanocomposite film via spray-coating of rare-earth strontium aluminate for anti-counterfeit applications. *Luminescence* **2021**, *36*, 1933–1944.

[17] Cao, T. M. D.; Le, T. T. G.; Turrell, S.; Ferrari, M.; Lam, Q. V.; Tran, T. T. V. Luminescent ink based on upconversion of $NaYF_4$:Er,Yb@MA Nanoparticles: Environmental friendly synthesis and structural and spectroscopic assessment. *Molecules* **2021**, *26*, 1041.

[18] Kanika; Kumar, P.; Singh, S.; Gupta, B. K. A novel approach to synthesise a dual-mode luminescent composite pigment for uncloneable high-security codes to combat counterfeiting. *Chem.—Eur. J.* **2017**, *23*, 17144–17151.

[19] Li, M. X.; Yao, W. J.; Liu, J.; Tian, Q. Y.; Liu, L.; Ding, J.; Xue, Q. W.; Lu, Q.; Wu, W. Facile synthesis and screen printing of dual-mode luminescent $NaYF_4$:Er,Yb (Tm)/carbon dots for anti-counterfeiting applications. *J. Mater. Chem. C* **2017**, *5*, 6512–6520.

[20] Zhou, S.; Wang, Y.; Hu, P.; Zhong, W.; Jia, H.; Qiu, J. R.; Fu, J. J. Cascaded photon confinement-mediated orthogonal RGB-switchable $NaErF_4$-cored upconversion nanoarchitectures for logicalized information encryption and multimodal luminescent anti-counterfeiting. *Laser Photon. Rev.* **2023**, *17*, 2200531.

[21] Liu, W. J.; Zhang, W. J.; Liu, R. X.; Li, G. J. Up-conversion of lanthanide ions and down-conversion defect luminescence in $BaGdF_5$:Yb,Er/Tm for application in anti-counterfeiting. *New J. Chem.* **2021**, *45*, 17377–17383.

[22] Liu, Y. S.; Tu, D. T.; Zhu, H. M.; Li, R. F.; Luo, W. Q.; Chen, X. Y. A strategy to achieve efficient dual-mode luminescence of Eu^{3+} in lanthanides doped multifunctional $NaGdF_4$ nanocrystals. *Adv. Mater.* **2010**, *22*, 3266–3271.

[23] Ding, Y. D.; Wu, F.; Zhang, Y. L.; Liu, X. M.; de Jong, E. M. L. D.; Gregorkiewicz, T.; Hong, X.; Liu, Y.; Aalders, M. C. G.; Buma, W. J. et al. Interplay between static and dynamic energy transfer in biofunctional upconversion nanoplatforms. *J. Phys. Chem. Lett.* **2015**, *6*, 2518–2523.

[24] Zhou, B.; Yang, W. F.; Han, S. Y.; Sun, Q.; Liu, X. G. Photon upconversion through Tb^{3+}-mediated interfacial energy transfer. *Adv. Mater.* **2015**, *27*, 6208–6212.

[25] Yan, L.; Zhou, B.; Song, N.; Liu, X. L.; Huang, J. S.; Wang, T.; Tao, L. L.; Zhang, Q. Y. Self-sensitization induced upconversion of Er^{3+} in core–shell nanoparticles. *Nanoscale* **2018**, *10*, 17949–17957.

[26] Chen, Q. S.; Xie, X. J.; Huang, B. L.; Liang, L. L.; Han, S. Y.; Yi, Z. G.; Wang, Y.; Li, Y.; Fan, D. Y.; Huang, L. et al. Confining excitation energy in Er^{3+}-sensitized upconversion nanocrystals through Tm^{3+}-mediated transient energy trapping. *Angew. Chem., Int. Ed.* **2017**, *56*, 7605–7609.

[27] Wang, Y. The role of an inert shell in improving energy utilization in lanthanide-doped upconversion nanoparticles. *Nanoscale* **2019**, *11*, 10852–10858.

[28] Adusumalli, V. N. K. B.; Lee, S. Y.; Gupta, A.; Park, Y. I. Upconversion and ligand-sensitized downshifting from active inert shell in Ln-doped core–shell nanocrystals for anticounterfeiting applications. *Mater. Today Chem.* **2023**, *34*, 101793.

[29] Jia, H.; Teng, Y. Y.; Li, N.; Li, D. G.; Dong, Y. H.; Zhang, D.; Liu, Z. H.; Zhao, D.; Guo, X. Y.; Di, W. H. et al. Dual stimuli-responsive inks based on orthogonal upconversion three-primary-color luminescence for advanced anticounterfeiting applications. *ACS Mater. Lett.* **2022**, *4*, 1306–1313.

[30] Li, X. M.; Guo, Z. Z.; Zhao, T. C.; Lu, Y.; Zhou, L.; Zhao, D. Y.; Zhang, F. Filtration shell mediated power density independent orthogonal excitations-emissions upconversion luminescence. *Angew. Chem., Int. Ed.* **2016**, *55*, 2464–2469.

[31] Prorok, K.; Bednarkiewicz, A.; Cichy, B.; Gnach, A.; Misiak, M.; Sobczyk, M.; Strek, W. The impact of shell host ($NaYF_4$/CaF_2) and shell deposition methods on the up-conversion enhancement in Tb^{3+}, Yb^{3+} codoped colloidal α-$NaYF_4$ core-shell nanoparticles. *Nanoscale* **2014**, *6*, 1855–1864.

[32] Qian, H. S.; Zhang, Y. Synthesis of hexagonal-phase core–shell $NaYF_4$ nanocrystals with tunable upconversion fluorescence. *Langmuir* **2008**, *24*, 12123–12125.

[33] Sotiriou, G. A.; Schneider, M.; Pratsinis, S. E. Color-tunable nanophosphors by co-doping flame-made Y_2O_3 with Tb and Eu. *J. Phys. Chem. C* **2011**, *115*, 1084–1089.

[34] Li, N. N.; Wen, X. Y.; Liu, J.; Wang, B. J.; Zhan, Q. Q.; He, S. L. Yb^{3+}-enhanced UCNP@SiO_2 nanocomposites for consecutive imaging, photothermal-controlled drug delivery and cancer therapy. *Opt. Mater. Express* **2016**, *6*, 1161–1171.

[35] Homann, C.; Krukewitt, L.; Frenzel, F.; Grauel, B.; Würth, C.; Resch-Genger, U.; Haase, M. $NaYF_4$:Yb,Er/$NaYF_4$ core/shell nanocrystals with high upconversion luminescence quantum yield. *Angew. Chem., Int. Ed.* **2018**, *57*, 8765–8769.

[36] Damasco, J. A.; Chen, G. Y.; Shao, W.; Ågren, H.; Huang, H. Y.; Song, W. T.; Lovell, J. F.; Prasad, P. N. Size-tunable and monodisperse Tm^{3+}/Gd^{3+}-doped hexagonal $NaYbF_4$ nanoparticles with engineered efficient near infrared-to-near infrared upconversion for *in vivo* imaging. *ACS Appl. Mater. Interfaces* **2014**, *6*, 13884–13893.

[37] Fujii, M.; Nakano, T.; Imakita, K.; Hayashi, S. Upconversion Luminescence of Er and Yb Codoped $NaYF_4$ Nanoparticles with Metal Shells. *J. Phys. Chem. C* **2013**, *117*, 1113–1120.

[38] Xie, S. W.; Tong, C.; Tan, H. H.; Li, N.; Gong, L.; Xu, J. X.; Xu, L. J.; Zhang, C. F. Hydrothermal synthesis and inkjet printing of hexagonal-phase $NaYF_4$: Ln^{3+} upconversion hollow microtubes for smart anti-counterfeiting encryption. *Mater. Chem. Front.* **2018**, *2*, 1997–2005.

[39] Wu, W. N.; Liu, H. Z.; Yuan, J.; Zhang, Z.; Wang, L.; Dong, S. L.; Hao, J. C. Nanoemulsion fluorescent inks for anti-counterfeiting encryption with dual-mode, full-color, and long-term stability. *Chem. Commun.* **2021**, *57*, 4894–4897.

[40] Xie, S. W.; Gong, G.; Song, Y.; Tan, H. H.; Zhang, C. F.; Li, N.; Zhang, Y. X.; Xu, L. J.; Xu, J. X.; Zheng, J. Design of novel lanthanide-doped core-shell nanocrystals with dual up-conversion and down-conversion luminescence for anti-counterfeiting printing. *Dalton Trans.* **2019**, *48*, 6971–6983.